

Investigating realistic anode off-gas combustion in SOFC/ICE hybrid systems: mini review and experimental evaluation

International J of Engine Research

1–17

© IMechE 2021

Article reuse guidelines:

sagepub.com/journals-permissions

DOI: 10.1177/14680874211058324

journals.sagepub.com/home/jer



Ioannis Nikiforakis¹, Zhongnan Ran¹ , Michael Sprengel², John Brackett²,
Guy Babbitt² and Dimitris Assanis^{1,3} 

Abstract

Solid oxide fuel cells (SOFCs) have been deployed in hybrid decentralized energy systems, in which they are directly coupled to internal combustion engines (ICEs). Prior research indicated that the anode tailgas exiting the SOFC stack should be additionally exploited due to its high energy value, with typical ICE operation favoring hybridization due to matching thermodynamic conditions during operation. Consequently, extensive research has been performed, in which engines are positioned downstream the SOFC subsystem, operating in several modes of combustion, with the most prevalent being homogeneous compression ignition (HCCI) and spark ignition (SI). Experiments were performed in a 3-cylinder ICE operating in the latter *modus operandi*, where the anode tailgas was assimilated by mixing syngas (H₂: 33.9%, CO: 15.6%, CO₂: 50.5%) with three different water vapor flowrates in the engine's intake. While increased vapor content significantly undermined engine performance, brake thermal efficiency (BTE) surpassed 34% in the best case scenario, which outperformed the majority of engines operating under similar operating conditions, as determined from the conducted literature review. Nevertheless, the best performing application was identified operating under HCCI, in which diesel reformates assimilating SOFC anode tailgas, fueled a heavy duty ICE (17:1), and gross indicated thermal efficiency ($\eta_{th,ig}$) of 48.8% was achieved, with the same engine exhibiting identical performance when operating in reactivity-controlled compression ignition (RCCI). Overall, emissions in terms of NO_x and CO were minimal, especially in SI engines, while unburned hydrocarbons (UHC) were non-existent due to the absence of hydrocarbons in the assessed reformates.

Keywords

Solid oxide fuel cell, internal combustion engine, multi-cylinder engine testing, spark ignition, hybrid power generation, anode tailgas

Date received: 18 June 2021; accepted: 10 October 2021

Introduction

Climate change has been identified among the most significant contemporary challenges,¹ especially when considering its accelerating rate.² As a result, mitigation efforts have been prioritized within a broad range of scientific disciplines.^{3,4} The particular spectrum includes past and ongoing research in the transportation sector, given its association to increased greenhouse gas (GHG) emissions, which are considered among the main contributors to global warming.⁴ Specifically, the over-consumption of fossil fuels has been established amid the main drivers of climate change⁵ and research has indicated that up to 20% of overall GHG emissions

are accounted to the particular sector.⁶ Therefore, ongoing environmental degradation has been partly attributed to conventional transportation practices,⁵ rendering both the establishment of stricter emission

¹Department of Mechanical Engineering, Stony Brook University, Stony Brook, NY, USA

²Czero, Fort Collins, CO, USA

³Institute for Advanced Computational Science, Stony Brook University, Stony Brook, NY, USA

Corresponding author:

Dimitris Assanis, Department of Mechanical Engineering, Stony Brook University, 100 Nicolls Rd, Stony Brook, NY 11794, USA.

Email: dimitris.assanis@stonybrook.edu

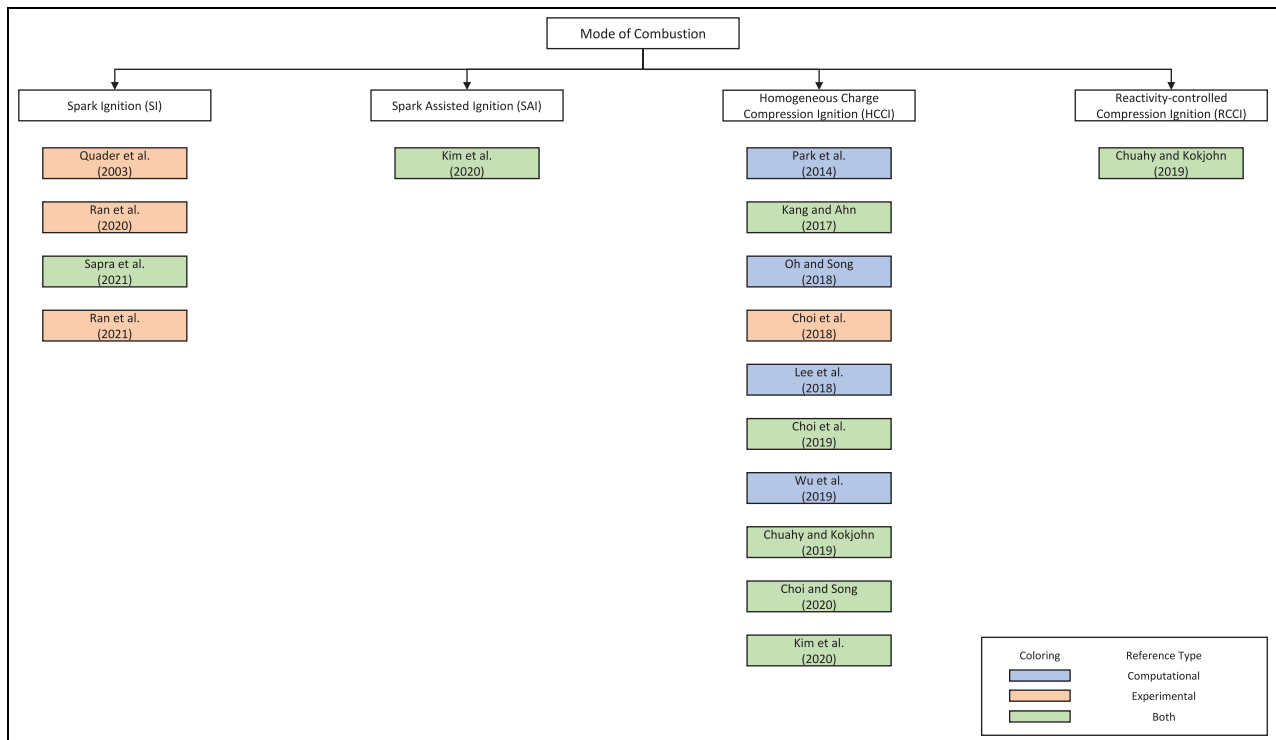


Figure 1. All identified research articles classified under different modes of combustion (MoCs) involving SI, SAI, HCCI, and RCCI, as adapted from.^{13,18,22,25,26,31–39}

limits⁷ as well as the introduction of novel technologies,⁸ among the core drivers of the respective response.

The emergence of innovative technologies in the transportation sector has been mainly identified in electric,⁹ hydrogen,¹⁰ and hybrid vehicles.¹¹ Research on the gradual electrification of passenger cars indicated that future projections, in respect to the number of electric vehicles (EVs), are expected to account for over a third of all circulating cars by 2030.¹² Meanwhile, vehicles running on hydrogen mainly operate on proton exchange membrane fuel cells (PEMFCs), in which reverse electrolysis results to current production being directed to the vehicle's electric motor.⁹ Additionally, electrochemical technologies were coupled with conventional internal combustion engine (ICE) operation, with the resulting systems shifting toward hybrid implementation. In that, a multitude of significant observations on ICE operation have accrued from research in alternate sectors, frequently correlating to decentralized energy production systems.¹³

Extended research has been performed on the latter, which mainly provide stationary power production by coupling ICEs to solid oxide fuel cells (SOFCs). The increased efficiency of those systems, in comparison to conventional energy production practices such as gas turbines (GTs), is principally due to high documented efficiencies of the SOFC, having been recorded over 70%.⁷ Nevertheless, it is in part relative to the absence of power transmission losses,¹⁴ due to their implementation in a decentralized manner. Furthermore, the load-following capability of either ICEs or turbomachinery,

makes for the inability of SOFCs to safely, and efficiently function under wide ranges of operating conditions,¹⁵ especially in part-load operation. Specifically, the cells cannot tolerate significant amounts of carbon deposition, since the latter will render the technology inoperable due to stack breakage. Given that fuel cell subsystems are provided with oxidant input at the desired pressure, incoming fuel should be reformed in either auxiliary external pre-reformers, internal reformers, or both. In case reforming is conducted internally, excess SOFC heat and steam will be used in the necessary endothermic reforming reactions, while cooling down the stack up to a point, and therefore lower the level of its degradation.¹⁶ The latter should additionally reduce the pumping work of cooling air directed to the stack, thus raising overall efficiency.¹⁷ In such a manner, the reformed fuel feed is conformed to desired fuel concentrations, as stipulated by the particulars of SOFC operation.^{18,19} Arguably, positioning of either GTs or ICEs upstream the SOFC stack, in terms of oxidant stream (cathode), in several occasions should notably enhance performance.^{15,20} On the other hand, consumed fuel (anode) consisting of various methane mixtures, culminates to anode tailgas. In turn, it is exploited in order to raise system efficiency, with a multitude of ways being reported. It could either be combusted in the aforementioned ICE components,²¹ preheat incoming anode fuel feed or auxiliary water streams directed to the reformer,²² and provide amounts of heat wherever required, as in reforming reactions, or in-between them combinations. Moreover, the absence of any

intermittency issues, linked to popular renewable energy (RE) technologies, such as wind turbines (WTs) and photovoltaic (PV) panels, are being dealt with hybridization with SOFC subsystems. Therefore, the particular type of systems should probably be favored over aforementioned stand-alone RE practices, at least in terms of stable and uninterrupted operation.^{23,24}

The ever growing popularity of the SOFCs in hybrid configurations, could be explained by several reasons, emerging though recent research and development. Primarily, SOFC operating conditions, such as temperature and pressure, favor hybridization with thermal equipment operating within a similar range, such as ICEs. In particular, the former conditions reportedly ranged from 600°C²⁵ to 1000°C,²¹ whereas the latter were documented in both pressurized²² and atmospheric²⁶ operation in the respective SOFCs. Atmospheric operation particularly allows for upstream positioning of ICEs, since the overall configuration is absolved from essential pumping work, where the engine would operate as an external reforming subsystem.²⁵ Furthermore, anode tailgas is rendered high in energy value, therefore enabling downstream direction and consequent combustion to an ICE subsystem. As a result, the complementary power production should exert a significant effect on overall performance.²⁰ In that, the thermodynamically rich off-gas is consumed in an ICE engine, rather than being disposed at the system's exhaust, with respective literature indicating gains in terms of system efficiency.²⁷ In fact, coupling with ICEs, may result to a better overall performance when compared to the most prominent SOFC hybrids (SOFC/GT), as engines have significantly improved overall efficiencies, as well as operate in a wider range of conditions.²⁶ In further detail, the relatively high cycle efficiencies of the SOFC were widely reported over 50% in terms of electrical efficiency and in the proximity of design-point-operation.²⁸ In certain cases they even surpassed the Carnot limit within a particular temperature range,²⁹ since maximum efficiency shifted from the Carnot limit to the Gibbs free energy over enthalpy of formation ratio. Hence, it benefited higher concentration of power production in the SOFC subsystem when examining hybrid configurations. Meanwhile, the minimal CO₂ emissions relative to SOFC operation were reportedly in agreement with established legislation to tackle ongoing climate change,³⁰ as well as enabled hybridization of technologies relating to fossil fuel consumption (ICE). The increased cost of the particular technology nevertheless should be considered,²⁰ even when expensive catalysts, frequently associated to its operation, were not deployed in the majority of cases.³¹

In terms of the ICE subsystems being integrated in the studied hybrid layouts, piston engines were implemented and rigorously examined in both computational and experimental frameworks. In detail, multiple modes of combustion were considered, enhancing system flexibility in operation, among which the most dominant

was identified in homogeneous charge compression ignition (HCCI).^{13,18,22,25,26,31–35} Other modes involved all spark ignition (SI),^{36–39} spark-assisted ignition (SAI),¹⁸ as well as reactivity-controlled compression ignition (RCCI).¹³ Evidently, low temperature combustion (LTC) was extensively assessed, with the majority of researchers investigating leaner mixtures,^{22,25} as illustrated in Figure 1 and in certain cases across multiple compression ratios (CRs).³⁷ Apparently, researchers compared different combustion modes for the same initial conditions, such as Chuahy and Kokjohn,¹³ who compared HCCI to RCCI *modi operandi*.

Overall, the frameworks developed in the aforementioned hybrid energy configurations provided information on ICEs, mainly running on natural gas (NG) reformates, and should significantly contribute in a relative comparison with hydrogen-based transportation. In that, the conduction of experiments in similar apparatus and under various operating conditions, would allow for consequent correlations with existing research on hybrid SOFC/ICE systems. As a result, valuable insights would be provided on the overall assessment of the potential associated to hydrogen-based ICE operation.

Literature review

The assessment of existing research articles should significantly aid toward establishing rigid standards of comparison for the investigated configurations. In relation to the latter, a total of 21 different research articles were identified, in which SOFC subsystems were coupled to ICEs, with the fuel cell stacks concentrating higher energy production across hybrid components. The particular publications were ordered chronologically in Tables 1 to 3, with a range of modes, features and operating conditions being documented in the former, as adapted from the cited articles. It should be mentioned that results of the experimental studies emerging from sections *Experimental methodology* and *Experimental results*, were listed in the same tables, to facilitate overall comparison. On that note, the *Discussion* section included rigorous correlations, between the current and aforementioned sections. In general, the reviewed hybrid systems operated mostly on NG, as was observed in all,^{7,13,18,22,25,26,31–35,37–41} and across a variety of mixture concentrations. Moreover, hydrogen was examined in dual fuel operation with diesel,²¹ as was methanol.^{11,42} Additionally, gasoline was used³⁶ whereas gasified woody biomass syngas was considered by Moriconi et al.,⁴³ in increasing carbon content sequence. Lastly, additional SOFC features involving all operating temperature and pressure, steam-to-carbon ratio, utilization factor and current density were listed in Table A1 of the Appendix, as adapted from cited literature.

In regard to the NG-fed hybrid configurations, there were three key studies of similar applications identified

Table 1. Main input variables identified on SOFC/ICE research, as adapted from cited literature.

Reference	Parent Fuel	Auxiliary Fuel	MoC	CR [–]	ϕ [–]	T_{in} [K]	SPT	EGR [%]
Quader et al. ³⁶	Gasoline	—	SI	9.5:1	0.38 to 0.68	—	MBT	—
	Gasoline	—	SI	9.5:1	1	—	MBT	17–37
Stobart and Chaudhari ¹¹	Methanol	Diesel	—	—	—	—	—	—
Chaudhari et al. ²¹	Hydrogen	Diesel	—	—	—	—	—	—
Chaudhari et al. ⁴²	Methanol	Diesel	—	—	—	—	—	26–30
Park et al. ²⁶	NG	—	HCCI	—	1	—	—	—
Moriconi et al. ⁴³	Biomass	—	HCCI	8.5:1	—	—	—	—
Fyffe et al. ⁷	Methane	—	LHR-CI	17:1	2	—	—	—
Luo et al. ⁴⁰	—	NG	—	—	—	—	—	—
Kang and Ahn ²²	NG	—	HCCI	8.2:1	1.0	—	—	—
Luo et al. ⁴¹	—	NG	—	—	—	—	—	—
Choi et al. ³¹	NG	—	HCCI	8.2:1	0.5–1	650–700	—	—
Oh and Song ²⁵	NG	—	HCCI	16:1	0.15 to 0.6	—	—	—
Lee et al. ³²	LNG	—	HCCI	16.9:1	—	—	—	—
Chuahy and Kokjohn ¹³	Diesel	—	HCCI	16.9:1	0.348 to 0.374	333	—	33
	Diesel	Diesel	RCCI	16.9:1	—	342	—	34.3
Choi et al. ³³	NG	—	HCCI	8.2:1	0.75	673	—	—
Wu et al. ³⁴	NG	Hydrogen	HCCI	—	—	—	—	—
Choi and Song ³⁵	NG	—	HCCI	8.2	—	—	—	—
Ran et al. ³⁷	NG	—	SI	11:1	0.6–1	—	MBT	—
	NG	—	SI	13:1	0.6–1	—	MBT	—
Kim et al. ¹⁸	Methane	—	SAI	8.2:1	—	563–663	–90 to –40 CAD (aTDC)	—
	Methane	—	HCCI	8.2:1	0.95	673 to 713	—	—
Sapra et al. ³⁸	NG	NG	SI	12:1	—	—	24 CAD (bTDC)	—
Ran et al. ³⁹	NG	—	SI	9:1	0.6–1	—	MBT	—
	NG	—	SI	11:1	0.6–1	—	MBT	—
	NG	—	SI	13:1	0.6–1	—	MBT	—
Current Work	NG	—	SI	10:1	0.6–1	350 K	MBT	—

in examined literature, mainly integrating atmospheric SOFCs (ASOFCs) to ICE subsystems. Primarily, Wu et al.,³⁴ Kim et al.,¹⁸ as well as Sapra et al.³⁸ assessed the hybridization of ASOFCs with ICE subconfigurations, with the overall system running on NG. In terms of the former, a steady-state thermodynamic model was implemented for a marine application, where a direct internal reforming SOFC (DIRSOFC) stack was coupled to an ICE, operating in HCCI mode. The Otto-cycle was used in order to simulate engine operation, with a pressure ratio of 4.4:1 being assumed, while the increased relative exergy loss (43.54%) and decreased power generation in the engine were addressed with auxiliary hydrogen addition. It is worth mentioning, that fuel supply was distinguished between parent and auxiliary fuel in Table 1. The former referred to the fuel being supplied to the overall hybrid system, while the latter accounted for direct provision to the ICE subsystem. Accordingly, auxiliary hydrogen³⁴ was streamed directly to the ICE, originating from the deployment of a metal hydride reactor (MHR), exploiting waste heat of exhaust gases. Out of all investigated scenarios, the case of an extra 20% hydrogen addition through the MHR resulted to optimal hybrid performance, while anode hydrogen recirculation significantly contributed to maximum efficiency. Albeit hydrogen addition, the base case

being assessed in the particular research article consisted of anode tailgas combustion under HCCI mode, whereas the auxiliary hydrogen should render it under dual fuel classification. Likewise, a similar type of system was developed for the reported simulations,¹⁸ although it was accompanied by experiments being carried out on a single-cylinder Honda GX390, conducted in order to validate the implemented hybrid model. Specifically, CR was fixed at 8.2:1, with both SAI and HCCI modes being considered for the assessed 5 kW system, as depicted in Table 1. The former modus operandi resulted to significantly lower coefficients of variance (COVs) for the assessed combustion, with the spectrum of the examined intake temperatures ranging from 290°C to 400°C. In particular, the former switched from over 30% (HCCI) to a range between 5% and 7% (SAI), mainly depending on combustion phasing. Additionally, indicated efficiency was increased by more than 8%, while emissions plummeted by more than 35% and 10%, in terms of CO and NO_x, respectively, at an intake temperature (T_{in}) reported at 400°C. Indicatively, the optimal net indicated mean effective pressure (IMEP_n) was 1.38 bar (Table 2), with CA50 being documented at 70 crank angle degrees (CAD) after top dead center (aTDC) (Table 3). Sapra et al.³⁸ investigated a marine system application incorporating an 8-cylinder boosted engine

Table 2. Main engine performance data from SOFC/ICE systems, as adapted from cited literature. Net and gross are indicated by (n) and (g) in the table, respectively.

Reference	$\eta_{th,i}$ [%]	$\eta_{f,i}$ [%]	IMEP [bar]	BTE [%]	η_v [%]
Quader et al. ³⁶	—	—	—	—	—
Stobart and Chaudhari ¹¹	—	—	—	—	—
Chaudhari et al. ²¹	—	—	—	—	—
Chaudhari et al. ⁴²	—	—	—	—	—
Park et al. ²⁶	—	—	—	—	—
Moriconi et al. ⁴³	—	—	—	—	—
Fyffe et al. ⁷	—	—	29.9–31.8 (n)	—	—
Luo et al. ⁴⁰	—	—	—	—	—
Kang and Ahn ²²	—	—	—	—	—
Luo et al. ⁴¹	—	—	—	—	—
Choi et al. ³¹	—	25–30 (g)	—	—	—
Oh and Song ²⁵	—	—	1.5–5 (g)	—	—
Lee et al. ³²	—	—	—	—	—
Chuahy and Kokjohn ¹³	48.8 (g)	—	9.4 (g)	—	—
	48.2 (g)	—	9.5 (g)	—	—
Choi et al. ³³	25.1 (n)	—	—	—	—
Wu et al. ³⁴	—	—	—	—	—
Choi and Song ³⁵	—	—	—	—	—
Ran et al. ³⁷	—	31 (n)	2.5 (n)	—	38
	—	31.2 (n)	3 (n)	—	35
Kim et al. ¹⁸	—	—	1.35–1.38 (n)	—	—
	—	—	0.88–1.5 (n)	—	—
Sapra et al. ³⁸	—	33–37 (n)	—	—	—
Ran et al. ³⁹	—	29.3–30.5 (n)	2.05–3.25 (n)	—	31.0–41.0
	—	29.3–31.0 (n)	2.00–3.20 (n)	—	31.5–42.5
	—	28.3–31.3 (n)	1.90–3.15 (n)	—	33.5–44.0
Current Work	—	—	4.75–7.50 (n)	31–34 (n)	37.5–46.5

that operated under a CR of 12:1.⁴⁴ They performed experiments in order to validate a Seiliger cycle-based in-cylinder submodel, developed in order to appropriately capture the H₂-CO₂-NG-blend in SI combustion. Maximum brake efficiency (η_b) peaked at 34.47% among the three cases used to validate the implemented model, for which the respective compositions amounted at 15% H₂, 15% CO₂, and 70% NG [vol]. Spark timing was maintained at 24 CAD before top dead center (bTDC) (Table 1) across all experiments, whereas the power split was optimized between SOFC and ICE components. Specifically, it resulted to a reduction of about 60% in terms of NO_x, 20.74% in respect to CO₂ and merely 43% in regard to unburned hydrocarbons (UHC). Lastly, among the three respective hybrid applications, as investigated in,^{18,34,38} the two former configurations exhibited better performance at their proposed optimal operation. Especially when comparing the systems identified between,^{34,38} where load requirements were comparable, operation under HCCI modus operandi seemed to outperform hybrid operation when integrating the SI engine. Nevertheless, no experiments were performed in the former, neither HCCI combustion was further assessed in order to render hybrid operation stable, as in the latter.

Pressurized SOFC (PSOFC) operation was additionally incorporated under similar configurations, for which extended information was identified in the

performed review. Primarily, Kang and Ahn²² examined a system in which a planar PSOFC stack was coupled to an ICE subsystem, for which dynamic modeling simulations were performed in MATLAB-Simulink, and later validated against respective experimental data. To specify, the latter were acquired for all PSOFC, HCCI engine as well as external reformer, with the ICE operating under a CR of 8.2:1. It should be mentioned, that the resulting simulations originated from a model based on modified knock-integral-approach to a map-based model. The authors concluded that in terms of the ICE, the engine sub-model could reach steady-state at every cycle during load alterations, with its operation being directly dependent to the specifics of anode tailgas. Furthermore, Choi et al.³¹ investigated the same core configuration, while an additional external reformer was deployed upstream of the SOFC anode. Both computational and experimental work were performed, where the engine, operating under HCCI mode, was dependent on six control variables in the former, relative to all flowrate, thermodynamic state, as well as composition of SOFC anode tailgas. Within the study's experimental framework, a modified Honda GX390 was deployed, at which a number of measurements were obtained for more than one fuel-air equivalence ratio (ϕ), accounting for the change in load conditions, based to aforementioned anode tailgas features. Particularly, experiments indicated that gross indicated fuel conversion efficiency

Table 3. Mass fraction burned (MFB) and emissions data on SOFC/ICE configurations, as adapted from cited literature.

Reference	CA10 [CAD]	CA50 [CAD]	CA10-90 [CAD]	NO _x	CO	UHC
Quader et al. ³⁶	15–40	—	20–40	0.8–8.0 [g/kWh]	1–13 [g/kWh]	0.5–1.5 [g/kWh]
	15–50	—	25–50	0.1–1.0 [g/kWh]	1–2 [g/kWh]	0.5–1.5 [g/kWh]
Stobart and Chaudhari ¹¹	—	—	—	—	—	—
Chaudhari et al. ²¹	—	—	—	—	—	—
Chaudhari et al. ⁴²	—	—	—	—	—	—
Park et al. ²⁶	—	—	—	—	—	—
Moriconi et al. ⁴³	—	—	—	—	—	—
Fyffe et al. ⁷	—	—	40	—	—	—
Luo et al. ⁴⁰	—	—	—	—	—	—
Kang and Ahn ²²	—	—	—	—	—	—
Luo et al. ⁴¹	—	—	—	—	—	—
Choi et al. ³¹	—	—	—	< 5 ppm	1000–2000 pm	—
Oh and Song ²⁵	—	—	—	—	—	—
Lee et al. ³²	—	—	—	—	—	—
Chuahy and Kokjohn ¹³	—	5.7	—	0.57 [g/kg _{fuel}]	131 [g/kg _{fuel}]	—
	—	5.2	—	0.81 [g/kg _{fuel}]	193 [g/kg _{fuel}]	—
Choi et al. ³³	—	—	—	< 1 [ppm]	1326 [ppm]	—
Wu et al. ³⁴	—	—	—	—	—	—
Choi and Song ³⁵	—	—	—	—	—	—
Ran et al. ³⁷	—	7	—	< 1 [g/kg _{fuel}]	< 30 [g/kg _{fuel}]	—
	—	10	—	< 1 [g/kg _{fuel}]	< 35 [g/kg _{fuel}]	—
Kim et al. ¹⁸	—	8.5–35.7	—	0.35–0.65 [ppm]	1897–3642 [ppm]	—
	—	7.0–16.8	—	0.54–0.58 [ppm]	2338–3095 [ppm]	—
Sapra et al. ³⁸	—	—	—	0.8–1.4 [g/kWh]	—	—
Ran et al. ³⁹	—	8.5–10.5	24.5–32.0	0.25–1.20 [g/kg _{fuel}]	20–30 [g/kg _{fuel}]	—
	—	6.0–8.0	25.5–34.5	0.15–1.10 [g/kg _{fuel}]	25–45 [g/kg _{fuel}]	—
	—	7.0–11.0	29.5–38.5	0.25–1.20 [g/kg _{fuel}]	35–65 [g/kg _{fuel}]	—
Current Work	—	—	1.6–12.8	—	—	—

($\eta_{f,ig}$) could reach 25% to 30%, while resulting NO_x would be less than 5 ppm (@ O₂ 15%). The combustion was justifiably stable, since the COV of gross indicated mean effective pressure (IMEP_g) was again in the neighborhood of 5%. Intake temperature nevertheless was required at a minimum of 600 K throughout the overall investigation. In that, Choi et al. concluded that in all experiments, IMEP_g should be at a minimum of 1.8 bar in order for the respective COV to be lower than 5%. Again, Choi et al.³³ identified the optimal design point for the aforementioned configuration,³¹ in terms of both performance and stability in operation. Particularly, they used the Cantera thermodynamic toolbox, and validated the proposed model for the particular design point of hybrid PSOFC/ICE operation, with the engine operating in HCCI mode and at a ϕ of 0.75 (Table 1). To continue, the application performed at a 59% overall efficiency, with the respective emissions at engine exhaust being measured lower than 1 ppm (@ O₂ 15%), in terms of both CO and NO_x. Withal, increased heat losses identified in ICE operation prompted Choi and Song³⁵ to propose the ‘composition-considered Woschni’ correlation and validate the suggested framework. In brief, it accounted for unusual mixture compositions at the engine’s intake, throughout several loading conditions. Meanwhile, Ran et al.³⁷ conducted an experimental study in which a

cooperative fuel research (CFR) engine was used in order to investigate SI operation. The engine was running on both compressed NG (CNG) and syngas, with the latter assimilating to SOFC anode tailgas. Throughout all conducted experiments, spark timing (SPT) was phased in order to achieve maximum brake torque (MBT) (Table 1). In that, maximum net indicated fuel conversion efficiency ($\eta_{f,in}$) of 31.2% was achieved for a CR of 13:1 with a ϕ of 0.9, whereas NO_x and soot emissions were justified negligible. Ran et al.³⁹ additionally investigated operating the same apparatus at CRs of 9:1, 11:1 and 13:1 (SI), with variable water vapor content, ranging from 0 to 50%. Net fuel conversion efficiency peaked at 31.3% for the latter CR, combustion efficiency was maximized at 97% for the former CR, while water vapor content over 30% significantly deteriorated operation. Fyffe et al.⁷ proposed both port fuel-injected (PFI) HCCI operation, in terms of low-temperature architectures, as well as direct-injection (DI) low-heat rejection compression ignition (LHR-CI), in regard to high-temperature system configurations. The latter complemented PSOFC/GT and PSOFC/GT/steam turbine (ST) subsystems with ICE subconfigurations, in an effort to assess whether the 70% threshold of energy efficiency could be surpassed in transportation-scale ICE hybridization. The highest performing system was investigated after

iterative simulations in the developed thermodynamic models, while the work produced at the ICE would account for 7% out of the total produced work. The PSOFC stack on the other hand, would produce the largest respective proportions at 61%. Lastly, Luo et al.^{40,41} examined a hybrid power system, accommodating all WT, PV, and ICE, apart from the reversible solid oxide fuel cell (RSOC) stack. It should be mentioned that the overall system was fueled by NG, while additionally incorporating battery storage, in an effort to evaluate RE technology penetration in decentralized configurations. Throughout the cited applications that integrated pressurized SOFC to engine operation, the highest overall system efficiency was identified in,⁷ where the respective system would reach 69.9%, in which the engine was reportedly working in LHR mode. The second best hybrid arrangement, in terms of efficiency, was investigated by Choi et al.,³³ in which the authors optimized their proposed configuration to achieve net efficiency of 59%. Again, the engine would operate in HCCI modus operandi.

Combined heat and power (CHP) applications were furthermore suggested by Park et al.²⁶ and Lee et al.,³² in which PSOFC and ICE were considered the main energy sources. The addition of an auxiliary heat recovery steam generator (HRSG) was used in order to exploit residual exhaust energy from outstreaming gases to steam, satisfying the thermal load being required. The former developed detailed electrochemical models as well as performed an economic analysis in order to estimate the levelized costs of electricity (LCOEs) involved. In terms of engine operation, HCCI was considered and the Otto-cycle was assumed, as the knock-integral-approach was once again adapted in order to predict auto-ignition timing. Results indicated that the particular hybrid configuration would not only perform better, but result to lower LCOEs when compared to PSOFC and PSOFC/GT applications. Lee et al.³² conducted exergetic and exergoeconomic analyses on the same core layout, ruling that albeit the greatest exergy destruction being located at the HCCI engine, the aforementioned conclusions²⁶ were reaffirmed. It is worth mentioning, that both applications exhibited similar overall net electrical efficiencies of 59.5%²⁶ and 58%,³² post-optimization. Notably, both ICE subsystems reportedly operated under HCCI modus operandi, with the former configuration outperforming both stand-alone SOFC and SOFC/GT compared arrangements.

Diesel and gasoline were additionally investigated in several hybrid configurations, when ICEs were coupled to SOFC stacks in decentralized power production practices. Quader et al.³⁶ pioneered gasoline reformates research in such applications, when experimentally assessing various levels of dilution in the mixture being directed to a single-cylinder CFR engine. In particular, they performed two sets of experiments, with results indicating that the deployment of a SOFC subsystem, upstream of the ICE, would dramatically increase overall efficiency. Furthermore, Chuahy and Kokjohn¹³

performed experiments on a Caterpillar C15 single-cylinder engine, in an attempt to identify optimal conditions for the developed 0-D electrochemical and equilibrium model of the hybrid system. In terms of hybrid system specifics, diesel was assumed as the parent fuel (Table 1), which was desulfurized and reformed prior to being directed to the SOFC stack. In turn, the produced anode tailgas was directed downstream to the 6-cylinder, 15 L engine. The developed model would implement the assessed HCCI mode of operation, while a bypass was introduced prior to diesel desulfurization. In that, a certain amount of fuel would be directly injected to the engine, and along with the anode tailgas would render the engine's mode of operation RCCI. In further detail, the experimental equipment stipulated that premixed syngas was supplied to the ICE through PFI, while CR was documented at 16.9:1. Overall, maximum electrical efficiency was identified for both RCCI and HCCI modes at 72.6% and 73.4%, respectively, in the aftermath of the conducted simulations. Simultaneously, the required experiments exhibited measurements for NO_x and CO that averaged at 0.81 g/kg_{fuel} and 193 g/kg_{fuel} for RCCI, and 0.57 g/kg_{fuel} and 131 g/kg_{fuel} for HCCI, respectively (Table 3). Gross indicated thermal efficiency ($\eta_{th,ig}$) was measured 48.2% and 48.8% between the RCCI and HCCI cases, with the respective IMEP_gs being computed at 9.5 and 9.4 bar, with all relative information being listed in Table 2. Notably, the hybrid configuration performed at the highest reported levels in terms of electrical efficiency, where the HCCI mode of operation resulted to an overall efficiency of 70.4% and integration of the RCCI ICE culminated to 69.7%.¹³

On top of the aforementioned modes of operation, additional dual fuel regimes were introduced across a number of research articles, in the same framework of hybrid integration between ICE and SOFC. Chaudhari et al.²¹ modeled a dynamic PSOFC/ICE hybrid application in MATLAB Simulink, in which the anode tailgas would be intercooled prior to the turbocharged 4-cylinder engine direction. At the same time, diesel would additionally be directly injected in a dual fuel scheme. Instead of exhaust gas recirculation (EGR), cathode exhaust recirculation was considered, which resulted to oxygen-to-fuel ratio being assumed in the respective calculations. Engine operation seemed to eventually be impacted by SOFC's utilization factor and its excess oxygen ratio, as anticipated. Moreover, Stobart and Chaudhari¹¹ investigated the same core configuration running on both methanol and diesel, and developed a model using QSS-TB from the Simulink toolbox, involving a boosted diesel with a variable-geometry turbocharger with EGR. They simulated drive cycles for two separate locations, in which increased hybridization of the SOFC to the ICE seemed to result to significantly greater gains. Likewise, Chaudhari et al.⁴² considered a model predictive controller (MPC) for the aforementioned application, in their effort to achieve optimal performance.

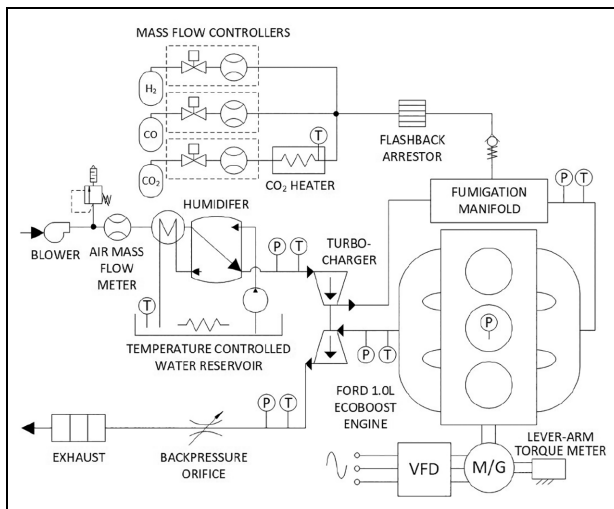


Figure 2. Test setup.

Experimental methodology

Testing of the multi-cylinder engine was conducted in such a way as to replicate, as close as practical, the conditions within an integrated SOFC/ICE system. Principally, this involved replicating the anode tailgas stream originating from the SOFC, modifying the engine to operate on the anode tailgas, and compensating for certain elements added for testing purposes. A schematic of the test setup (omitting various supporting components for clarity) is shown in Figure 2, while the core features of all relevant sensors are included in Table A2 of the Appendix.

A Ford Fox EcoBoost 1.0 L 3-cylinder engine was used for the multi-cylinder testing, with the engine's main features being enlisted in Table 4, while the included valve events account for cylinder 2. Selected modifications included:

- A fumigation manifold was added to mix the anode tailgas and air before entering the cylinders.
- The throttle was removed to reduce pumping losses, instead of air flowrate was controlled by adjusting engine speed.
- The fuel injectors were removed and plugged.
- An in-cylinder pressure transducer/spark plug replaced the existing spark plug in cylinder 2.
- The stock engine control unit (ECU) was replaced by a custom ECU.

Three characteristics of the anode tailgas stream were of principal interest and replicated: gas composition/flowrate, water flowrate, and temperature. The three constituent gasses of the tailgas stream (H_2 , CO , CO_2) were mixed on-site using calibrated mass flow controllers at a rate of 0.168 g/s (33.9% mole fraction) H_2 , 1.073 g/s (15.6% mole fraction) CO , and 5.423 g/s (50.5% mole fraction) CO_2 . The gas composition/flowrate was considered fixed as it originated from the SOFC and was held constant for all test cases.

Table 4. Engine specifications.

Engine specification	Quantity
Number of cylinders	3
Number of valves	4
Stroke	82 [mm]
Bore	71.9 [mm]
Displacement	998.8 [cm ³]
Clearance volume	36.9 [cm ³]
Compression ratio	10:1
Inlet valve opening (IVO)	5° (aTDC)
Inlet valve closing (IVC)	232° (aTDC)
Exhaust valve opening (EVO)	228° (bTDC)
Exhaust valve closing (EVC)	0° (aTDC)
Engine speed	Variable

Anode tailgas originating from a SOFC during operation will contain a large percentage of water due to the electrochemical reactions within the stack; more water than is permissible for reliable and efficient SI combustion. As such, a percentage of the water originating from the stack will need to be removed from the tailgas stream, by using a condenser before supplying the fuel stream to the engine. To determine the influence of water content on the engine's operation, the water content was varied from 0.15 to 0.75 g/s (3.4% to 17.0% mole fraction of the tailgas stream). This was accomplished by using a Nafion humidifier, located at the engine's intake air stream and controlling the temperature of the water circulating through the humidifier. By using the measured mass flowrate of incoming ambient air, and fully saturating that air at a controllable temperature (which directly sets the absolute humidity), the mass flowrate of water into the system was controlled. Notably, while this is not an exact recreation of how the engine would operate in a combined SOFC/ICE system, the air/fuel charges entering the cylinders are equivalent once the humidified air and dry fuel are mixed in the fumigation manifold. This approach also introduced additional heat into the system which aided in replicating the heat, provided by the anode tailgas stream. In particular, the humidification approach resulted in additional heat being introduced into the system via the incoming air and water, as they must both be heated to a minimum temperature which is required to achieve the desired fully-saturated conditions. The three main mechanisms which drive the heat input are the sensible heat of the water added, the water's heat of vaporization, and sensible heat of air which must be heated to the water's temperature. All things considered, three water vapor flowrates (0.30, 0.49, and 0.73 g/s) were selected in data illustration of all Figures 4 to 7.

The anode tailgas stream, after passing through the various recuperators, turbomachinery, and condensers will reach the engine at approximately 350 K, in terms of temperature. In addition to the heated water source that was used to control water flowrate in the intake air

stream, a second controlled heater was included on the CO_2 stream, to provide additional heat into the system. Based on the mass flowrate and temperature of the inlet air stream, the CO_2 heater was controlled, such that the air/fuel mixture would achieve the temperature resulting from the 350 K fuel stream mixing with inlet air.

The dyno consisted of a permanent magnet electric motor/generator connected to a high-performance variable frequency drive (VFD). The electric motor was operated in speed control mode, at the speed required to obtain the desired air flowrate. Therefore, it automatically transitioned between motoring and generating modes, based on the engine's net torque. This electric motor was mounted on trunnion bearings, with a lever arm torque meter providing torque measurements for the brake metrics. Moreover, indicated metrics were derived using an in-cylinder pressure transducer in cylinder 2, coupled with a 0.2° resolution encoder. To compensate for the pressure drop across the Nafion humidifier, as well as the testing facilities' $\sim 1,500\text{ m}$ elevation, a blower was used to supply air to the engine. The latter was controlled to achieve a nominal pressure equivalent to sea level at the engine's intake. Similarly, an orifice was included on the engine's exhaust to introduce backpressure, in order to compensate for the lower ambient pressure at altitude. Due to the potentially hazardous nature of the compressed H_2 and CO used for testing, the engine and experimental setup were housed in an ISO container-based dyno cell. The multi-cylinder engine in the dyno cell, isolated from Czero's main facility for safety, is shown in Figure 3.

Three parameters were adjusted during engine testing to determine the engine's optimal operating point: water flowrate, spark timing, and ϕ . Four water flowrates were evaluated during testing, by adjusting the humidifier's water temperature: 0.15, 0.30, 0.49, and 0.73 g/s. For each of these water flowrates, ϕ was varied between 0.6 and 1, by adjusting the engine's operating speed (rather than via an intake air throttle which would have introduced additional losses), while maintaining a constant fuel flowrate. Indicatively, for a ϕ of 0.6, this corresponded to an engine speed of 2400 rpm (13.8 g/s dry air), while a ϕ of 1 corresponded to an engine speed of 1650 rpm (8.4 g/s dry air), with the fuel flowrate (including CO_2) being 6.7 g/s. Finally, for each water/ ϕ combination, spark timing was adjusted to achieve MBT.

Experimental results

Brake mean effective pressure

Brake mean effective pressure (BMEP) is defined as the mean effective pressure (MEP) calculated from the actual measured brake torque output during combustion, independent of its displacement, while mechanical efficiency of the engine is accounted for. Figure 4 presents the multi-cylinder engine BMEP characteristics as a function of both ϕ and water vapor flow rates. As

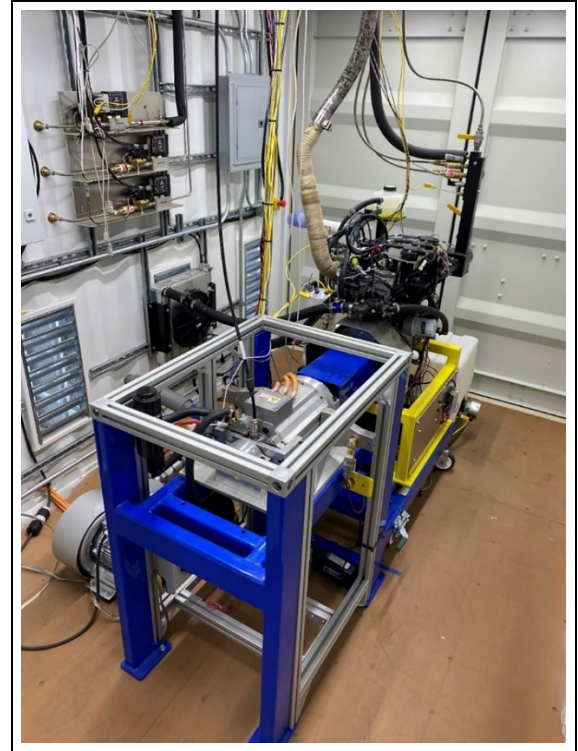


Figure 3. Multi-cylinder engine in Czero's dyno cell.

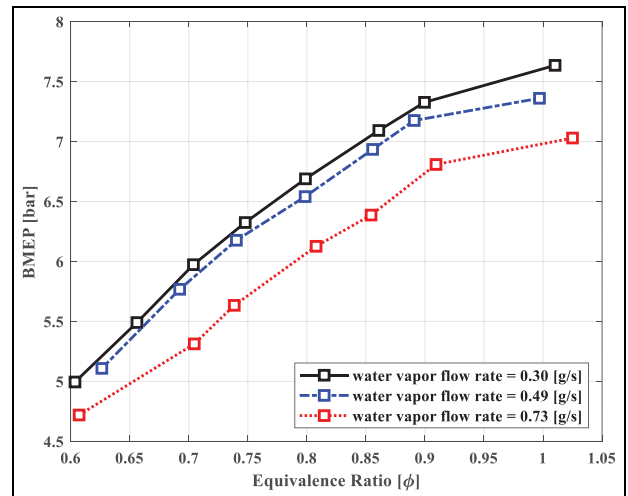


Figure 4. Engine brake mean effective pressure (BMEP) as a function of ϕ and water vapor flow rates.

shown in Figure 4, BMEP is proportionally increasing as ϕ is increased from 0.6 to stoichiometry, for all three of the water vapor flow rates. This is mainly due to the increased energy content for the air-fuel mixture, given that ϕ is increased. Therefore, the higher laminar flame speed caused the higher heat release rates during the combustion process. Consequently, that culminated to higher cylinder pressure and temperature, which in turn increased BMEP. On the other hand, increase in the water vapor flow rates has negatively impacted the engine output performance, as shown in the figure. As water vapor flow rate is increased from 0.30 to 0.73 g/s,

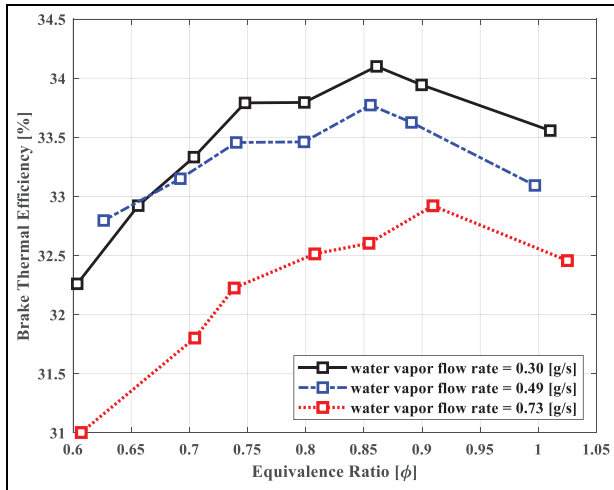


Figure 5. Engine brake thermal efficiency (BTE) as a function of ϕ and water vapor flow rates.

the engine's BMEP is significantly decreased, as a result of decreased combustion rates caused by the reduced laminar flame speed. It can be concluded from the same figure that increased presence of water vapor, at the studied levels, is detrimental to the engine output performance.

Brake thermal efficiency and brake specific fuel consumption

Figures 5 and 6 represent the brake thermal efficiency (BTE) and brake specific fuel consumption (BSFC) of the multi-cylinder engine for the anode tailgas combustion. As shown in Figure 5, lowering the ϕ from the stoichiometric condition caused an increase in BTE at first. Progression in even leaner conditions caused the latter to decrease, as ϕ is leaned out further away from stoichiometry. On the other hand, the trend is exactly the opposite in Figure 6, given that BSFC is inversely correlated to the BTE during the combustion process. As ϕ is initially driven leaner than stoichiometry, an increase in the ratio of specific heats (γ) along with a decrease in the heat transfer losses, resulted to an increase in terms of BTE and a decrease in terms of BSFC. However, as ϕ is further leaned out from stoichiometry, the decreased combustion rates caused by the slower laminar flame speed, reduce the peak combustion pressure and temperature, which detracts combustion stability. The occurrence of misfires and incomplete combustion negatively affect BTE, and therefore BSFC. Moreover, as illustrated in the aforementioned figures, as water vapor flow rate increases, BTE is considerably decreased, with BSFC being largely increased. Evidently, the particular trend can be attributed to the slower heat release rates, resulting from lower laminar flame speeds. The latter are naturally caused by the increased water vapor content in the fuel compositions.

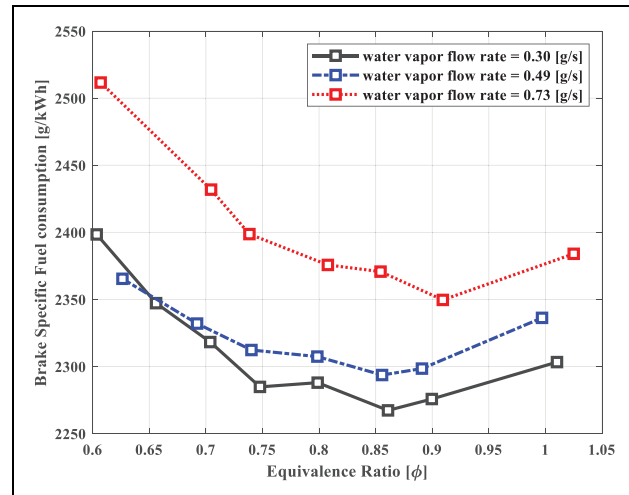


Figure 6. Engine brake specific fuel consumption (BSFC) - inclusive of diluents - as a function of ϕ and water vapor flow rates.

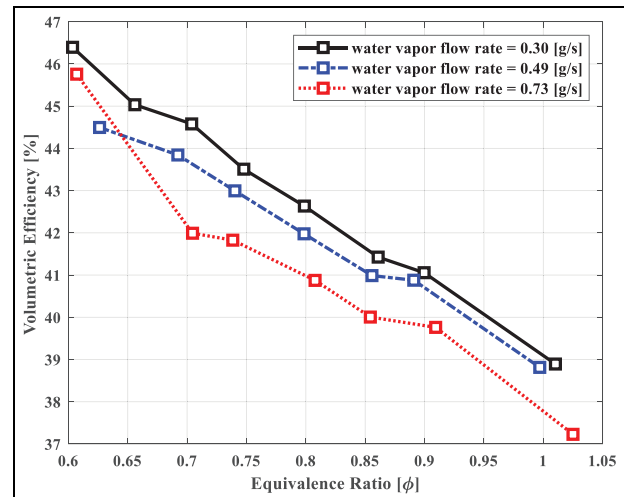


Figure 7. Volumetric efficiency as a function of ϕ and water vapor flow rates.

Volumetric efficiency

The engine's volumetric efficiency (η_v) is a parameter which is used to describe the effectiveness of the engine's breathing capacity during the intake stroke. Figure 7 presents the engine's volumetric efficiency, in respect to both the ϕ and the water vapor flow rates. As depicted in Figure 7, the volumetric efficiency in anode tailgas combustion is significantly lower than in combustion with conventional gasoline and compressed natural gas (CNG) fuels. That can be attributed to its very low lower heating value (LHV) and stoichiometric air-fuel ratio. Therefore, a significant amount of intake air was displaced during the intake process, which in turn caused the volumetric efficiency to be significantly lower. Moreover, it is evident in the figure that volumetric efficiency is increased as ϕ becomes leaner, due to the reduced fuel flow rate, and consequently, the

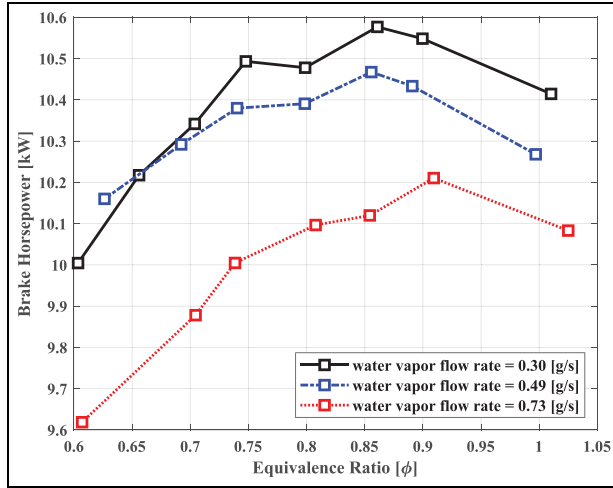


Figure 8. Break horsepower (BHP) as a function of ϕ and water vapor flow rates.

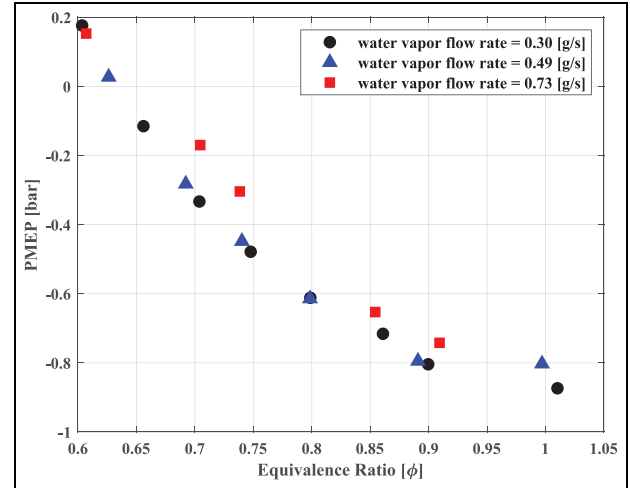


Figure 10. Pumping mean effective pressure (PMEP) as a function of ϕ and water vapor flow rates.

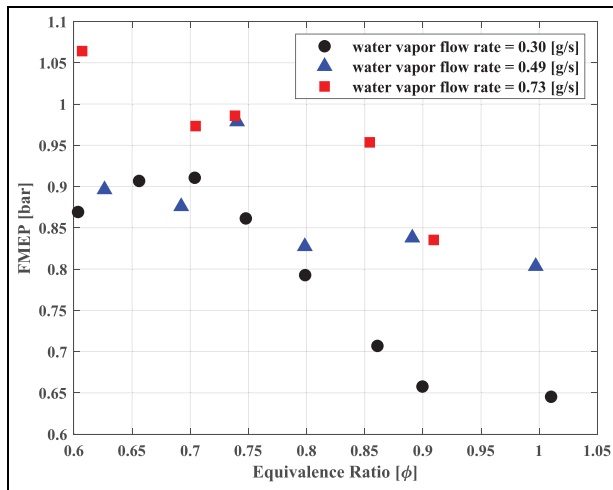


Figure 9. Friction mean effective pressure (FMEP) as a function of ϕ and water vapor flow rates.

increasing intake air flow rate. Lastly, increased water vapor flow rate is leading to reduced volumetric efficiency at the same ϕ , since a surge in water vapor will displace more of the intake air during the intake stroke.

Discussion

Considerable information was identified in the reviewed literature of section *Literature review*, relating to all performance and emissions in engine operation. In certain cases, it was deemed directly comparable to the experimental results of section *Experimental results*. On that regard, correlations between the aforementioned data should provide valuable insight on preferable operating frameworks.

The effects of both ϕ and water vapor flow rates on the engine brake horsepower (BHP) are presented in Figure 8. BHP is defined as the power measured using

a brake type dynamometer at specific engine operating conditions, and it represents the actual engine horsepower output, since engine friction losses are subtracted from the indicated engine horsepower. As shown in the figure, BHP is monotonically increasing as ϕ is increased from its lean misfire limit to around 0.9, for all of water vapor flow rates investigated. As ϕ is raised, the overall energy density of the air-fuel mixtures trapped in the combustion chamber is also increased. In turn, engine combustion rates are improved, and consequently, resulting higher cylinder peak pressure and temperature ensure greater engine power output. However, increasing the water vapor flow rates negatively impacts the engine output performance, as illustrated in the same figure, given that BHP is lower for higher water vapor flow rates. Naturally, introducing additional water vapor to the fuel content reduces the overall energy density of the in-cylinder mixtures, contributing to lower engine power output.

The friction mean effective pressure (FMEP), as a function of both ϕ and water vapor flow rates, is presented in Figure 9. FMEP is used to quantify the frictional losses during engine operation, and is defined as the difference between the indicated work and the actual brake work output. As shown in the figure, as ϕ is increased from the lean misfire limit to the stoichiometric condition, FMEP reduces in magnitude, as a result of the decreased engine speed, given that engine friction is highly dependent on the latter. Additionally, increasing the water vapor flow rates culminated to greater FMEPs, especially at the water vapor flow rate of 0.73 g/s. The particular trend can be attributed to the decreased cylinder peak pressure and temperature, which negatively affected the viscosity of the engine lubricant oil.

Figure 10 shows the pumping mean effective pressure (PMEP) of the multi-cylinder engine as a function of both ϕ and water vapor flow rates. PMEP is defined

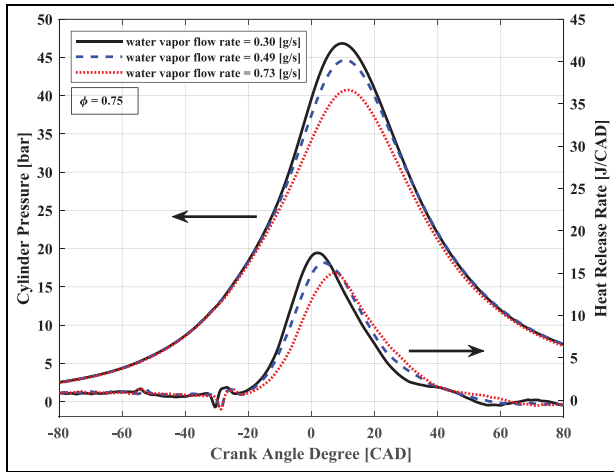


Figure 11. Cylinder pressure and heat release rate as a function of ϕ and water vapor flow rates.

as the effective pressure by exchanging air in and out of the engine cylinder across the intake and exhaust valves. It can be calculated by finding the difference between the net and gross indicated mean effective pressure. As shown in the figure, PMEP decreases in magnitude as ϕ increases from the lean misfire point to stoichiometry, and for all three water vapor flow rates. On the other hand, increasing water vapor flow rates from 0.3 to 0.49 g/s, exerted minimal effects on PMEP, whereas even greater water vapor flow rates (0.73 g/s) resulted in higher PMEP losses.

The effects of water vapor flow rate on the engine cylinder pressure and heat release rate at a ϕ of 0.75 are shown in Figure 11. It is illustrated that as the water vapor flow rate is increased from 0.30 to 0.73 g/s, both cylinder pressure and heat release rate are decreased in magnitude. The particular effect is attributed to the presence of the water vapor in the SOFC tailgas fuel content that reduces its energy density, as well as its laminar flame speed. Therefore, increasing the water vapor flow rate resulted in lower cylinder peak pressure and energy heat release during combustion at the same engine operating conditions.

In terms of the effects of ϕ on the engine heat release rate, at the same water vapor flow rate of 0.30 g/s during combustion, they are evident in Figure 12. As presented in the respected graph, decreasing ϕ resulted in lower energy heat release rate during the combustion process, which is mainly due to the reduction in the overall energy content of the trapped air-fuel mixture in the cylinder per cycle. Thus, decreased laminar flame speeds caused by the overall leaner mixture yielded decreased combustion rates.

Apart from the analysis emerging from the experimental results, as illustrated in all Figures 8 to 12, significant observations were made in the aftermath of the conducted literature review. In terms of performance, the highest efficiency was reported by Chuahy and Kokjohn¹³ at 48.8% and in gross indicated terms

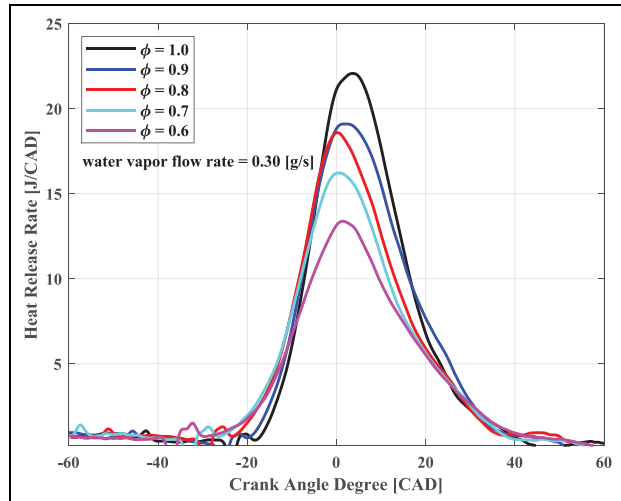


Figure 12. Heat release rate plotted against crank angle degree, when water vapor flow rate is fixed at 0.30 g/s.

(Table 2), for an HCCI engine with a CR of 16.91:1 (Table 1), for which intake pressure was maintained at 3.9 bar. While ϕ ranged between 0.35 and 0.37 for the diesel reformat mixture and EGR was fixed at 33%, IMEP_g was the second highest recorded among all reviewed research articles, computed at 9.4 bar (Table 2). Apparently, the highest value was again identified¹³ for the same engine operating in RCCI mode, where additional fuel would be injected at 800 bar, with the start of injection (SOI) being determined at -45 CAD (aTDC). Resulting IMEP_g was estimated 9.5 bar, whereas respective efficiency was approximated 48.2%. While the rest of the recorded data, relative to the respective experiments, were listed in all Tables 1 to 3, the next better-performing engines involved the configuration examined by Choi et al.³¹ They rigorously investigated HCCI operation of an application running on NG reformates, in which throughout all variations, gross indicated fuel conversion efficiency ranged between 25% and 30%. Moreover, Choi et al.³³ concluded that optimal operation for their proposed design, was achieved at thermal efficiency of 25.1%, where again the engine operated in HCCI modus operandi, at a CR of 8.2:1 (Tables 1 and 2). In addition, 31.3% net indicated fuel conversion efficiency was determined by Ran et al.^{37,39} for a CFR engine operating under a CR of 13:1 (SI), running on SOFC anode tailgas (anhydrous), with concentrations of 33.9% H₂, 15.6 CO and 50.5% CO₂. In any case, BTE values being determined in the performed experiments of sections *Experimental methodology* and *Experimental results*, arguably surpassed both aforementioned values. Even in the greatest water vapor flow case, BTE peaked between 32.5% and 33% (Figure 5), whereas the investigated apparatus definitely under-performed when compared to the experimental framework examined by Chuahy and Kokjohn.¹³ Indeed, information on the mass fraction burned (MFB) between the two

cases was included in Table 3, in which evidently the latter registered significantly shorter CA50, estimated at 5.7 CAD (HCCI) and 5.2 CAD (RCCI), in contrast to the 7 CAD and 10 CAD of the former.

Performance of the ICE subsystem would naturally impact hybrid efficiency, with a number of respective correlations being observed in the aftermath of the conducted literature review. The best performing hybrid configurations were the ones integrating the ICE subsystems which exhibited the highest reported efficiencies, as analyzed in the study of Chuahy and Kokjohn.¹³ Additionally, in these hybrid configurations that operated on diesel provision, the HCCI engine performed marginally better than the RCCI ICE, with the particular trend being repeated in hybrid performance. The identification of HCCI in the best performing systems was noticed throughout the majority of assessed applications, and over several operating conditions. When the SOFC stack operated under ambient pressure and the overall arrangement was NG-fed, the schemes integrating HCCI engines^{18,34} outperformed the respective SI hybrid applications.³⁸ Similarly, the phenomenon propagated throughout pressurized SOFC operation, where the HCCI mode of operation was identified in the ICE of the second best-performing hybrid system, with the respective net efficiency reaching 59%. The best performing system in the particular category implemented a complex structure under a significantly greater load than the rest of the reviewed configurations, and incorporated a LHR mode of operation. Apart from the aforementioned power systems, CHP applications involved HCCI ICE subsystems among their best-performing configurations, with net electrical efficiency reaching 59.5%.²⁶

In relation to reported emissions, the better-performing configurations investigated by Chuahy and Kokjohn¹³ exhibited NO_x and CO concentrations amounting at 0.57 and 131 g/kg_{fuel} (HCCI), as well as 0.81 and 193 g/kg_{fuel} (RCCI), respectively. NO_x emissions were shown to be minimal in the experiments performed by Ran et al.,³⁷ in which they were identified below 1 g/kg_{fuel}. CO exhaust concentrations were reportedly measured even lower than in,¹³ situated below the 35 g/kg_{fuel} threshold, for both CRs being investigated. Again, NO_x emissions were increasingly similar in the study performed by Ran et al.³⁹ while CO emissions were reported to increase for the higher CRs, peaking at 65 g/kg_{fuel}. The aforementioned configurations examined by Choi et al.³³ exhibited values below 1 ppm (@ O_2 15%) for the former and 1326 ppm (@ O_2 15%) for the latter, as illustrated in Table 3. SAI and HCCI operation resulted in similar emission ranges, as enlisted in the same table under Kim et al.¹⁸ Quader et al.³⁶ assessed engine operation under different dilution levels of bottle gas, as well as several gasoline reformates. They additionally examined both variable equivalence ratio near the lean limit (LL) with no EGR, as well as fixed stoichiometry with variable

EGR. The latter seemed to favor lower emissions, since maximum dilution seemed to exponentially decrease NO_x emissions, with the respective limits being depicted in Table 3. Overall, the particular research article seemed to be the sole piece of research reporting on UHC figures, ranging from 0.5 to 1.5 g/kWh throughout all recorded experiments.

Conclusions

Extensive research on hybrid configurations involving solid oxide fuel cells (SOFCs) and internal combustion engines (ICEs) among their core primary sources has been identified, providing valuable insight on hydrogen use in the latter. The similarity among the thermodynamic states required in the working fluids among the two technologies favored direct hybridization, which features exhibited high combined efficiencies as well as low emissions of all CO_2 , CO, and NO_x . Resulting configurations were mainly implemented in decentralized power systems, operating on parent fuels such as natural gas (NG), gasoline and diesel. Fuel streams were primarily reformed accordingly, through both external and internal (to the SOFC stack) reformers, and then redirected for SOFC consumption. They eventually resulted to anode tailgases of increased thermodynamic value, which combusted in ICEs positioned downstream of the cell stack; thus, enhancing overall system performance while producing minimal emissions. In that, auxiliary injections of all hydrogen, NG and diesel were additionally recorded, while detailed computational and experimental work was reported among reviewed literature. The specific information, along with performed experiments, culminated to significant observations relative to ICE characteristics, throughout the imposition of vast ranges of operation. A summary of the main findings follows:

1. Brake thermal efficiency (BTE) of the ICE in the performed experiments peaked at equivalence ratios (ϕ) ranging between 0.85 and 0.9 in examined operation, where the engine was running on combined mixtures of syngas and water vapor mixtures. In particular, the former constituted of all H_2 , CO, and CO_2 , with respective mole concentrations of all 33.9%, 15.6% and 50.5%, mixing in the engine's intake port with water vapor flows of all 0.3, 0.49 and 0.73 g/s, resulting to SOFC anode tailgas assimilation. In the spark ignition (SI) modus operandi of the experiments, existing literature exhibited directly comparable performance data, in which the assessed configurations nevertheless did not outperform the 3-cylinder engine deployed in the experiments. Naturally, while increased water vapor reduced BTE as well as shifted peak efficiency to greater ϕ , unthrottled operation and greater volumetric efficiency (η_v) seemed to favor the investigated ICE, when compared to the reviewed experiments.
2. The best performing applications nevertheless involved homogeneous charge compression

ignition (HCCI) as well as reactivity-controlled compressed ignition (RCCI) engine operation, as identified in the reviewed literature. In the former, gross indicated thermal efficiency ($\eta_{th,ig}$) reached 48.8%, with the ICE running on lean diesel reformat ($\phi \sim 0.36$). Detailed in-cylinder composition involved inert gases that amounted at 72.1% (N_2) and 15.5% (CO_2), while O_2 , H_2O , H_2 , and CO were reported at 16.7%, 3.4%, 4.3%, and 2.0%, respectively. In the latter case, $\eta_{th,ig}$ was approximated at 48.2% and diesel was simultaneously directly injected, apart from the port-fuel-injected (PFI) diesel reformat mixture which was previously mentioned. As a result, greater NO_x and CO emissions were reported in the RCCI mode of operation. In any case, combustion was deemed stable in both cases, with respective coefficients of variance (COVs) amounting at 3% and 2% in terms of gross indicated mean effective pressure (IMEP_g). The particular stability was achieved when operating under HCCI above a certain intake temperature threshold ($\sim 400^\circ C$), below which they functioned under spark-assisted ignition (SAI).

3. Hybrid configurations integrating ICE subsystems that operated in HCCI mode outperformed the engine subconfigurations which implemented other modes of operation. The sole exceptions to the particular trend consisted of complex schemes that integrated additional gas turbines (GTs) and steam turbine bottoming cycles. In the specific hybrid applications, the ICE operated in low-heat rejection, compression-ignition (LHR-CI) mode. In all other reviewed cases, in which either ambient or pressurized SOFC stacks were coupled to ICE subconfigurations, and operated on either NG or diesel parent fuel feeds, the HCCI-ICE-integrating hybrids outperformed their SI counterparts. Notably, the highest documented electrical efficiency in SOFC/ICE systems operating in HCCI modus operandi reached 70.4% (system power $\sim 1.1 MW_e$), with the aforementioned LHR-CI-integrating arrangement achieving an efficiency of 69.9% (IMEP ~ 32 bar).
4. Reviewed emissions in the respective literature mainly involved reporting on NO_x and CO , since unburned hydrocarbon (UHC) concentrations were non-existent in exhaust gases, due to the absence of hydrocarbons in the assessed fuel reformates. The former naturally increased in higher peak cylinder temperatures, especially when operating in HCCI mode, with increased exhaust gas recirculation (EGR) nevertheless being deployed to mitigate the phenomenon. In most examined cases, the particular concentrations were reported under 1 g/kg_{fuel} , apart from lower-dilution gasoline reformates with no EGR. CO concentrations were relatively low, due to both overwhelmingly lean mixtures being combusted, as well as the previously mentioned absence of hydrocarbons.

Declaration of conflicting interests


The author(s) declared no potential conflicts of interest with respect to the research, authorship, and/or publication of this article.

Funding

The work was supported by the United States Department of Energy under ARPA-E INTEGRATE project DE-AR0000959 that was awarded to and led by Stony Brook University.

ORCID iDs

Zhongnan Ran  <https://orcid.org/0000-0001-5813-3293>

Dimitris Assanis  <https://orcid.org/0000-0001-5506-806X>

References

1. Baldinelli A, Cinti G, Desideri U and Fantozzi F. Biomass integrated gasifier-fuel cells: experimental investigation on wood syngas tars impact on NiYSZ-anode solid oxide fuel cells. *Energy Convers Manag* 2016; 128(361–370): 361–370.
2. Tong S and Ebi K. Preventing and mitigating health risks of climate change. *Environ Res* 2019; 174(February): 9–13.
3. Tvinnereim E, Fløttum K, Gjerstad Ø, Johannesson MP and Nordø ÅD. Citizens' preferences for tackling climate change. Quantitative and qualitative analyses of their freely formulated solutions. *Glob Environ Change* 2017; 46(May): 34–41.
4. Kang JN, Wei YM, Liu LC, Han R, Yu BY and Wang JW. Energy systems for climate change mitigation: a systematic review. *Appl Energy* 2020; 263(February): 114602.
5. Abas N, Kalair A, Khan N and Kalair AR. Review of GHG emissions in Pakistan compared to SAARC countries. *Renew Sustain Energy Rev* 2017; 80(January 2016): 990–1016.
6. Li M, Rao AD and Scott Samuelsen G. Performance and costs of advanced sustainable central power plants with CCS and H_2 co-production. *Appl Energy* 2012; 91(1): 43–50.
7. Fyffe JR, Donohue MA, Regalbuto MC and Edwards CF. Mixed combustion–electrochemical energy conversion for high-efficiency, transportation-scale engines. *Int J Engine Res* 2017; 18(7): 701–716.
8. Abdin Z, Zafaranloo A, Rafiee A, Mérida W, Lipiński W and Khalilpour KR. Hydrogen as an energy vector. *Renew Sustain Energy Rev* 2020; 120(November 2019): 109620.
9. Song D, Zhang X, Neagu R and Qu W. Techno-economic analysis and feasibility study of a solid oxide fuel cell-battery hybrid system for water taxi application. *J Electrochem Energy Convers Storage* 2019; 16(2): 1–13.
10. Schock HAROLDJ and Oppenheim ANTONIK. Raison d'être of fuel cells and hydrogen fuel for automotive powerplants. In: *SAE 2004 world congress & exhibition*, SAE International, Detroit, MI, USA, March 2004.
11. Stobart RICHARDK and Chaudhari ANITAR. A novel hybrid powerplant for passenger bus applications. In: *Powertrain & fluid systems conference and exhibition*, SAE International, Rosemont, IL, USA, October 2007.

12. Gómez Vilchez JJ, Jochem P and Fichtner W. Interlinking major markets to explore electric car uptake. *Energy Policy* 2020; 144(January): 111588.
13. D.f. Chuahy F and Kokjohn SL. Solid oxide fuel cell and advanced combustion engine combined cycle: A pathway to 70% electrical efficiency. *Appl Energy* 2019; 235(November 2018): 391–408.
14. Akkaya A, Sahin B and Huseyinerdem H. An analysis of SOFC/GT CHP system based on exergetic performance criteria. *Int J Hydrogen Energy* 2008; 33(10): 2566–2577.
15. Traverso A, Magistri L and Massardo AF. Turbomachinery for the air management and energy recovery in fuel cell gas turbine hybrid systems. *Energy* 2010; 35(2): 764–777.
16. Dolenc B, Vrecko D, Juricic D, Pohjoranta A, Kiviaho J and Pianese C. Soft sensor design for estimation of SOFC stack temperatures and oxygen-to-carbon ratio. *ECS Trans* 2015; 68(1): 2625–2636.
17. van Biert L, Visser K and Aravind PV. A comparison of steam reforming concepts in solid oxide fuel cell systems. *Appl Energy* 2020; 264(C): DOI: 10.1016/j.apenergy.2020.114748
18. Kim J, Kim Y, Choi W, Ahn KY and Song HH. Analysis on the operating performance of 5-kW class solid oxide fuel cell-internal combustion engine hybrid system using spark-assisted ignition. *Appl Energy* 2020; 260: 114231.
19. Wang X, Lv X and Weng Y. Performance analysis of a biogas-fueled SOFC/GT hybrid system integrated with anode-combustor exhaust gas recirculation loops. *Energy* 2020; 197: 117213.
20. Buonomano A, Calise F, d'Accadia MD, Palombo A and Vicidomini M. Hybrid solid oxide fuel cells–gas turbine systems for combined heat and power: A review. *Appl Energy* 2015; 156: 32–85.
21. Chaudhari A, Plianos A and Stobart R. Modeling and control design of a SOFC-IC engine hybrid system. *SAE Technical Papers* 2008; (724):776–790. DOI: 10.4271/2008-01-0082
22. Kang S and Ahn KY. Dynamic modeling of solid oxide fuel cell and engine hybrid system for distributed power generation. *Appl Energy* 2017; 195: 1086–1099.
23. Luta DN and Raji AK. Decision-making between a grid extension and a rural renewable off-grid system with hydrogen generation. *Int J Hydrogen Energy* 2018; 43(20): 9535–9548.
24. Frigo S and Spazzafumo G. Comparison of different system layouts to generate a substitute of natural gas from biomass and electrolytic hydrogen. *Int J Hydrogen Energy* 2020; 45(49): 26166–26178.
25. Oh S and Song HH. Exergy analysis on non-catalyzed partial oxidation reforming using homogeneous charge compression ignition engine in a solid oxide fuel cell system. *Int J Hydrogen Energy* 2018; 43(5): 2943–2960.
26. Park SH, Lee YD and Ahn KY. Performance analysis of an SOFC/HCCI engine hybrid system: system simulation and thermo-economic comparison. *Int J Hydrogen Energy* 2014; 39(4): 1799–1810.
27. Diskin D and Tartakovsky L. Efficiency at maximum power of the low-dissipation hybrid electrochemical–otto cycle. *Energies* 2020; 13(15): 3961.
28. Badur J, Lemański M, Kowalczyk T, Ziółkowski P and Kornet S. Zero-dimensional robust model of an SOFC with internal reforming for hybrid energy cycles. *Energy* 2018; 158: 128–138.
29. Larminie J and Dicks A. *Fuel cell systems explained*. John Wiley & Sons, Ltd, Chichester, UK, 2003. pp.25–43.
30. Choudhary T. Thermodynamic assessment of SOFC-ICGT hybrid cycle: Energy analysis and entropy generation minimization. *Energy* 2017; 134: 1013–1028.
31. Choi W, Kim J, Kim Y, Kim S, Oh S and Song HH. Experimental study of homogeneous charge compression ignition engine operation fuelled by emulated solid oxide fuel cell anode off-gas. *Appl Energy* 2018; 229(March): 42–62.
32. Lee YD, Ahn KY, Morosuk T and Tsatsaronis G. Exergetic and exergoeconomic evaluation of an SOFC-Engine hybrid power generation system. *Energy* 2018; 145(810–822): 810–822.
33. Choi W, Kim J, Kim Y and Song HH. Solid oxide fuel cell operation in a solid oxide fuel cell–internal combustion engine hybrid system and the design point performance of the hybrid system. *Appl Energy* 2019; 254: 113681.
34. Wu Z, Tan P, Zhu P, et al. Performance analysis of a novel SOFC-HCCI engine hybrid system coupled with metal hydride reactor for H₂ addition by waste heat recovery. *Energy Convers Manag* 2019; 191: 119–131.
35. Choi W and Song HH. Composition-considered Woschni heat transfer correlation: Findings from the analysis of over-expected engine heat losses in a solid oxide fuel cell–internal combustion engine hybrid system. *Energy* 2020; 203: 117851.
36. Quader AA, Kirwan JE and James Grieve M. Engine performance and emissions near the dilute limit with hydrogen enrichment using an on-board reforming strategy. In *SAE 2003 world congress & exhibition*, SAE International, Detroit, MI, USA, March 2003.
37. Ran Z, Assanis D, Hariharan D and Mamalis S. Experimental Study of Spark-Ignition Combustion Using the Anode Off-Gas from a Solid Oxide Fuel Cell. *SAE Technical Papers* 2020; 2020: 1–8.
38. Sapra H, Stam J, Reurings J, et al. Integration of solid oxide fuel cell and internal combustion engine for maritime applications. *Appl Energy* 2021; 281(August 2020): 115854.
39. Ran Z, Longtin J and Assanis D. Investigating anode off-gas under spark-ignition combustion for soft-ice hybrid systems. *Int J Engine Res* 2021. <https://doi.org/10.1177/14680874211016987>
40. Luo Y, Shi Y, Zheng Y, Gang Z and Cai N. Mutual information for evaluating renewable power penetration impacts in a distributed generation system. *Energy* 2017; 141: 290–303.
41. Luo Y, Shi Y, Zheng Y, Gan Z and Cai N. Strategy for Renewable Energy Storage in a Dynamic Distributed Generation System. *Energy Proc* 2017; 105: 4458–4463.
42. Chaudhari A, Plianos A and Stobart R. Development of model predictive controller for SOFC-IC engine hybrid system. *SAE Technical Papers* 2009; 2(1): 56–66.
43. Moriconi N, Laranci P, D'Amico M, et al. Design and preliminary operation of a gasification plant for micro-CHP with internal combustion engine and SOFC. *Energy Proc* 2015; 81(298–308): 298–308.
44. Sapra H, Godjevac M, De Vos P, Van Sluijs W, Linden Y and Visser K. Hydrogen-natural gas combustion in a marine lean-burn SI engine: A comparative analysis of Seiliger and double Wiebe function-based zero-dimensional modelling. *Energy Convers Manag* 2020; 207(January): 112494.

Appendix

Table A1. Main SOFC operating variables, identified through research on SOFC/ICE hybrids, as adapted from cited literature.

Reference	Parent fuel	Operating temperature [K]	Operating pressure [bar]	Steam-to-carbon ratio [-]	Utilization factor [%]	Current density [mA/cm ²]
Quader et al. ³⁶	Gasoline	—	—	—	—	—
	Gasoline	—	—	—	—	—
Stobart and Chaudhari ¹¹	Methanol	—	—	—	—	—
Chaudhari et al. ²¹	Hydrogen	—	—	—	> 70	—
Chaudhari et al. ⁴²	Methanol	—	—	—	70–95	—
Park et al. ²⁶	NG	1123	1.013	3.0	75	500
Moriconi et al. ⁴³	Biomass	—	—	—	—	—
Fyffe et al. ⁷	Methane	1273	—	—	85	—
Luo et al. ⁴⁰	—	—	—	—	—	—
Kang and Ahn ²²	NG	—	—	3.0	70	—
Luo et al. ⁴¹	—	—	—	—	—	—
Choi et al. ³¹	NG	—	—	2.5	65–75	—
Oh and Song ²⁵	NG	1073	1.013	—	70	—
Lee et al. ³²	LNG	1123	1.013	3.0	75	—
Chuahy and Kokjohn ¹³	Diesel	—	1	—	—	200
	Diesel	—	1	—	—	200
Choi et al. ³³	NG	—	—	2.5	65	—
Wu et al. ³⁴	NG	1073	1.013	2.5	—	—
Choi and Song ³⁵	NG	—	—	—	60–80	—
Ran et al. ³⁷	NG	—	—	—	68	—
	NG	—	—	—	68	—
Kim et al. ¹⁸	Methane	1023	—	2.5	70	—
	Methane	1023	—	2.5	70	—
Sapra et al. ³⁸	NG	1073	1.013	2	70–85	500
Ran et al. ³⁹	NG	—	—	—	68	—
	NG	—	—	—	68	—
	NG	—	—	—	68	—
Current Work	NG	—	—	—	68	—

Table A2. Main features of all relevant sensors in the experimental apparatus that was used.

Equipment	Parameter	Sensor type	Measurement range	Accuracy	Sensor make/model
H ₂ flow counter	H ₂ mass flowrate	Thermal mass flowmeter	0–165 SLPM	±1% FS	Sierra 100
CO flow counter	CO mass flowrate	Thermal mass flowmeter	0–7.5 SLPM	±1% FS	Sierra 100
CO ₂ flow counter	CO ₂ mass flowrate	Thermal mass flowmeter	0–271 SLPM	±2% FS	Sierra 100
Air flow counter	Inlet air flowrate	Thermal mass flowmeter	0–0.2 kg/s	±0.2% FS	Fox thermal FT2A
CO ₂ thermocouple	CO ₂ temperature	Type K thermocouple	–270°C to 1260°C	±2.2°C or ±0.75%	Omega type K
Engine thermal switch	Engine coolant temperature	Type K thermocouple	–270°C to 1260°C	±2.2°C or ±0.75%	Omega type K
Fuel mixture thermocouple	Fuel mixture temperature	Type K thermocouple	–270°C to 1260°C	±2.2°C or ±0.75%	Omega type K
Fumigation manifold thermocouple	Fumigation manifold temperature	Type K thermocouple	–270°C to 1260°C	±2.2°C or ±0.75%	Omega type K
Pre-turbo thermocouple	Exhaust temperature (pre-turbo)	Type K thermocouple	–270°C to 1260°C	±2.2°C or ±0.75%	Omega type K
Post-turbo thermocouple	Exhaust temperature (post-turbo)	Type K thermocouple	–270°C to 1260°C	±2.2°C or ±0.75%	Omega type K
Pre-turbo compressor thermocouple	Inlet temperature (pre-turbo compressor)	Type K thermocouple	–270°C to 1260°C	±2.2°C or ±0.75%	Omega type K
Humidifier tank thermocouple	Humidifier tank water temperature	Type K thermocouple	–270°C to 1260°C	±2.2°C or ±0.75%	Omega type K
Ambient thermocouple	Ambient temperature	Type K thermocouple	–270°C to 1260°C	±2.2°C or ±0.75%	Omega type K
Pre-turbo compressor pressure transducer	Inlet pressure (pre-turbo compressor)	Piezoresistive pressure transducer	0–30 psig	±0.5% FS	Omega RX199
Fumigation manifold pressure transducer	Fumigation manifold pressure	Piezoresistive pressure transducer	0–30 psig	±0.5% FS	Omega RX199
Fuel mixture pressure transducer	Fuel mixture pressure	Piezoresistive pressure transducer	0–150 psig	±0.5% FS	Omega RX199
In-cylinder pressure transducer	In-cylinder pressure	Piezoresistive pressure transducer	0–200 psig	±0.5% FS	Kistler 6115C
Pre-turbo pressure transducer	Exhaust pressure (pre-turbo)	Piezoresistive pressure transducer	0–30 psig	±0.5% FS	Omega RX199
Post-turbo pressure transducer	Exhaust pressure (post-turbo)	Piezoresistive pressure transducer	0–30 psig	±0.5% FS	Omega RX199
Dyno position sensor	Engine crank angle	Relative angle encoder	0.2°	–	Koyo TRDA-20
Dyno	Engine torque	Level arm load cell	±155 Nm	±0.05% FS	Interface SSMF
Humidity sensor	Ambient humidity	Capacitive humidity	5%–95% RH	±4% FS	Omega HX71-MA